Journal of Sound and Vibration (2002) **256**(3), 433–445
doi:10.1006/jsvi.2001.4217, available online at http://www.idealibrary.com on IDEAL®

ON THE HORN EFFECT OF A TYRE/ROAD INTERFACE, PART II: ASYMPTOTIC THEORIES

C.-Y. Kuo, R. A. G. Graf, A. P. Dowling and W. R. Graham

Cambridge University Engineering Department, Trumpington Street, Cambridge CB2 1PZ, England.
E-mail: apd1@eng.cam.ac.uk

(*Received* 26 *January* 2001, *and in final form* 3 *December* 2001)

In Part I, it was shown that boundary element method calculations could successfully be applied to determine sound amplification by a tyre/road geometry. However, the computations are expensive, limited to frequencies below 2500 Hz, and provide little physical insight. In Part II, two supplementary asymptotic approaches are developed; a ray theory for high frequencies and a compact body scattering model for low frequencies. When tested on a representative tyre geometry, these methods are found to have excellent predictive capabilities, at frequencies above 3 kHz and below 300 Hz respectively. Furthermore, the ray theory shows that the neglect of curvature in Ronneberger's wedge model (1989 *Workshop on Rolling Noise Generation, Institut fur Technische Akustik, Technische Universitat, Berlin*) leads to erroneous amplification levels and interference effects, and the scattering model intriguingly predicts that low frequency amplification increases with belt width independently of the tyre diameter. Lastly, this work confirms the importance of numerical calculations for the intermediate frequencies, where tyre noise is most significant.

1. INTRODUCTION

In Part I of this work, the boundary element method (BEM) was found be an effective tool for calculating the horn amplification of a tyre on a road. However, although the calculations have excellent predictive capabilities, they give little physical insight into the phenomenon. They also become increasingly demanding at higher frequencies. Thus, in Part II, the aim is to develop complementary asymptotic theories of the horn effect, applicable to low- and high-frequency regions of the spectrum.

A first attempt at an analytical description of the horn effect was made by Ronneberger [1]. He represented the tyre geometry as a flat rigid surface extending to infinity at a small angle to the road, forming a wedge-shaped horn. Contributions from a single source and its images then sum to produce a far-field acoustic pressure spectrum which exhibits a characteristic, lobed interference pattern. The finite width of the tyre is accounted for by superimposing a low-frequency dependence derived from the spectrum of a decaying sine wave. Although this model describes the general shape of the amplification spectrum, it does not fully resolve the low frequency behaviour, nor does it predict the correct lobe structure for high frequencies. It therefore seems necessary to describe the tyre geometry more accurately.

From the comparisons of experimental measurements and numerical results in references [2, 3], Graf *et al.* concluded that the geometric details of the tyre edges and side walls are unimportant. Additionally, the application of typical axle loads to the tyre only slightly affects the amplification rate. However, the finite width and curvature of the tyre belt are

0022-460X/02/$35.00

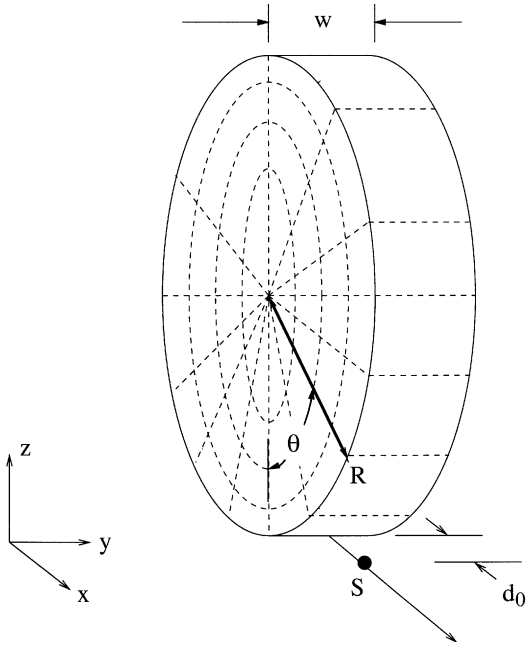

Figure 1. The simplified tyre model and discretization of the tyre surface (see section 3).

features which probably do need to be accounted for. Accordingly, the tyre is represented as a short cylinder with rigid surfaces (Figure 1). The radius of the cylinder is R and it has length (i.e., belt width) w.

In this asymptotic revisit of the horn effect, the broadband frequency range of interest is divided into two regions. For high frequencies, ray theory (see, for example, Keller [4]), is applied to illustrate the effects of surface curvature. Here, the sound emitted from the source is modelled as acoustic rays, which reach a far-field observer either directly, or via one or more reflections at the tyre and road surfaces. The multiple reflections of these rays are described by a set of recursive formulae which can be solved numerically. The resultant sound pressure is the linear superposition of contributions from individual rays, which are calculated by applying conservation of acoustic energy flux along the infinitesimally thin ray tubes. When a ray tube is reflected by a surface, the local curvature around the reflection point modifies the ratio of area change along the tube according to the mirror laws. This leads to a correction factor on the wave amplitude as a function of the curvature. The theory is described, and its predictions compared with experiment, in section 2. (See also Appendix A.)

At low frequencies, the tyre is treated as a simple acoustic scatterer. This leads to a multipole expansion for the acoustic far field. In addition to the prescribed monopole sound source, a dipole term appears, due to the presence of the tyre boundary. Its strength is linearly proportional to the acoustic frequency and the incompressible force exerted on the tyre due to the monopole. The predictions of this low-frequency analysis are compared with measurement and with BEM calculations in section 3.

2. HIGH-FREQUENCY RAY MODEL

As discussed above, the tyre is modelled as a rigid cylinder with radius R and belt width w, in contact with an infinite plane surface. Figure 1 shows this geometry, with a point

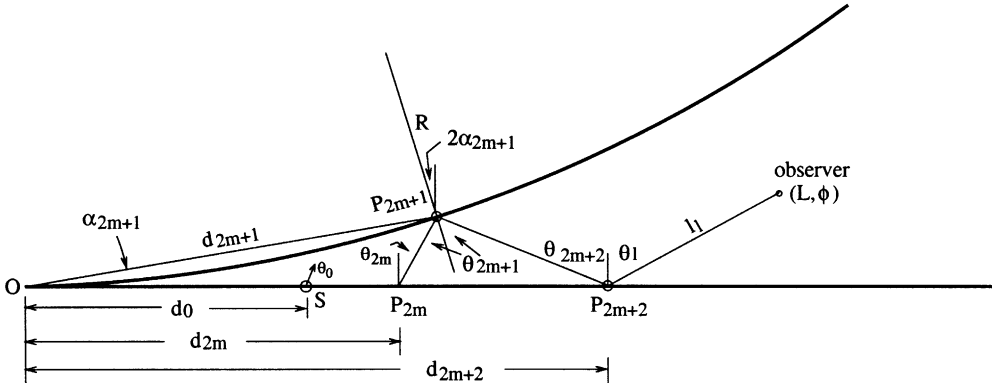

Figure 2. A ray of multiple reflections in the tyre/road pinch area.

source of sound, S, located a distance d_0 from the middle point of the tyre/road contact line. The observer position is at a distance L and angle ϕ to the road, as indicated in Figure 2. Both source and observer lie in the same xz plane for simplicity, and sound travels between the two along straight paths (rays). Incidence angles θ_{2m} and θ_{2m+1} are defined as the angles between the incident ray and the normals to the road and wedge surfaces respectively. The subscripts also indicate the number of reflections.

At the reflection point P_{2m+1} on the cylinder, the ray has undergone an odd number $2m+1$ of reflections, and the distance to the contact line is d_{2m+1} with a secant angle α_{2m+1}. The radius to P_{2m+1} is thus at an angle $2\alpha_{2m+1}$ to the vertical, so the incidence angles at successive reflections are related by

$$\theta_{2m+1} = \theta_{2m} + 2\alpha_{2m+1} \tag{1}$$

and

$$\theta_{2m+2} = \theta_{2m+1} + 2\alpha_{2m+1}. \tag{2}$$

The distances to reflection points can be linked by applying the sine rule to the triangles $OP_{2m}P_{2m+1}$ and $OP_{2m+1}P_{2m+2}$, yielding

$$\frac{d_{2m+1}}{\cos\theta_{2m}} = \frac{d_{2m}}{\cos(\theta_{2m} + \alpha_{2m+1})} \tag{3}$$

and

$$\frac{d_{2m+2}}{\cos(\alpha_{2m+1} + \theta_{2m+1})} = \frac{d_{2m+1}}{\cos\theta_{2m+2}}. \tag{4}$$

When combined with the relation $d_{2m+1} = 2R\sin\alpha_{2m+1}$, these equations can be applied in the order (3), (1), (4), (2) to find θ_{2m+2} for a given θ_{2m}. The final reflection angle, θ_{2M} (or θ_{2M+1} if the last reflection is from the cylinder), can thus be determined straightforwardly given the initial emission angle, θ_0.

The angle between the last reflection point and the observer, θ_l, follows again from the sine rule:

$$\frac{d_{2M}}{\cos(\theta_l + \phi)} = \frac{L}{\cos\theta_l} \tag{5}$$

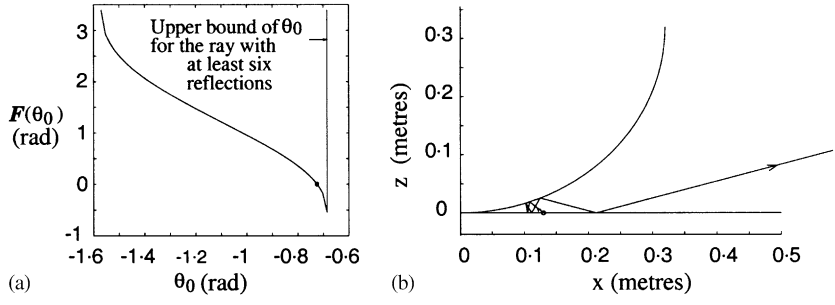

Figure 3. The ray of six reflections, $d_0 = 130$ mm and $(L, \phi) = (2{\cdot}8\text{ m}, 15^\circ)$. (a) $F(\theta_0)$; (b) the ray, $\theta_0 = -41{\cdot}5^\circ$.

or

$$\frac{d_{2M+1}}{\cos(2\alpha_{2M+1} + \theta_l - \phi)} = \frac{L}{\cos(\alpha_{2M+1} + \theta_l)} \tag{6}$$

if the last reflection is on the cylinder. Of course this reflection, like all previous ones, must have equal incidence and reflection angles, so that θ_l has to satisfy the constraint

$$F(\theta_0) = 0, \tag{7}$$

where

$$F(\theta_0) = \theta_l - \theta_{2M} \tag{8}$$

for a final reflection on the road, and

$$F(\theta_0) = \theta_l - \theta_{2M+1} \tag{9}$$

otherwise. In addition, θ_n is between $-\pi/2$ and $\pi/2$ for all values of n, and the last segment of the ray must not be obstructed by the cylinder.

A typical $F(\theta_0)$ is plotted in Figure 3(a) for a ray of six reflections. In all numerical results, the tyre radius is 32 cm. In this case, the sound source and the listener are at $d_0 = 130$ mm and $(L, \phi) = (2{\cdot}67\text{ m}, 15^\circ)$ respectively. The plot shows that the function $F(\theta_0)$ is a monotonically decreasing function of θ_0, so constraint (7) is satisfied only for one value, in this case $-0{\cdot}725$ rad $\simeq -41{\cdot}5^\circ$ (circled in the figure). (Figure 3(b) shows a visual check of this ray. It first propagates in towards the contact line before being reflected outward by the horn geometry.) Thus, for a given number of reflections, there is a unique solution for the emission angle θ_0 at the source. Furthermore, it is also found that no solution for θ_0 exists above a certain number of reflections, whose value depends on the source and observer locations.

As for the wedge case [5] then, there are only a finite number of rays which contribute to the sound at a given location. The amplitude of each contribution is derived from energy conservation along the ray tube (see Appendix A). For this calculation, the lengths of the ray segments shown in Figure 2 are required; these are straightforwardly obtainable once the d_n and θ_n have been calculated. On summing the contributions, the acoustic pressure at the observer is found, and the horn amplification follows from dividing by the corresponding pressure without the cylinder in place.

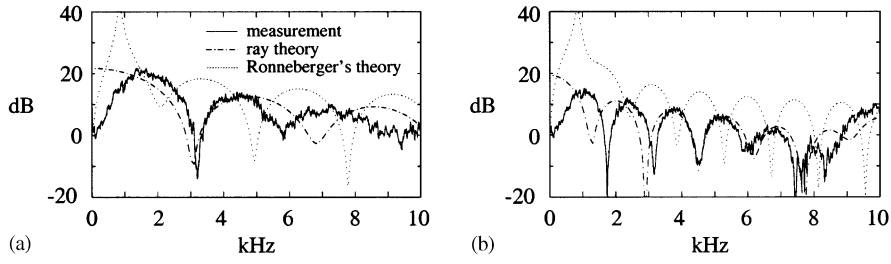

Figure 4. Comparison of transfer functions with cylindrical drum measurements. $(L, \phi) = (2{\cdot}8\text{ m}, 15^\circ)$. The sound source is at (a) $d_0 = 60$ mm and (b) $d_0 = 120$ mm.

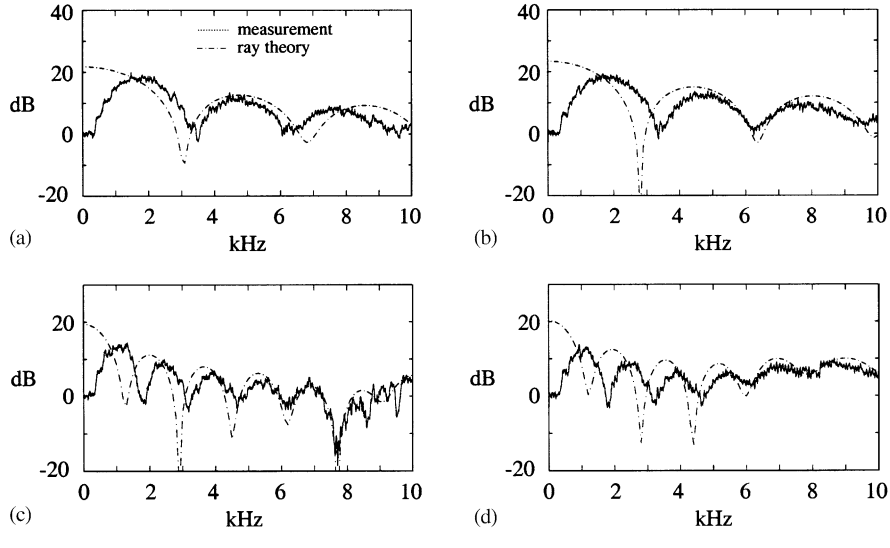

Figure 5. Comparison of transfer functions with smooth tyre measurements. (a) $d_0 = 60$ mm, $(L, \phi) = (2{\cdot}67\text{ m}, 15^\circ)$; (b) $d_0 = 60$ mm, $(L, \phi) = (1{\cdot}92\text{ m}, 2{\cdot}4^\circ)$; (c) $d_0 = 120$ mm, $(L, \phi) = (2{\cdot}67\text{ m}, 15^\circ)$; and (d) $d_0 = 120$ mm, $(L, \phi) = (1{\cdot}92\text{ m}, 2{\cdot}4^\circ)$.

Figure 4 shows comparisons between these calculations and measurements. The predictions of Ronneberger's wedge theory are also superimposed for reference. One of the difficulties in employing this theory is the choice of wedge angle. However, it is found that only the magnitude of the amplification is sensitive to this parameter when it is small; the dips in the spectrum remain fixed at the same frequencies. Here a wedge angle of 10° is used. It is clear that better agreement is achieved by using ray theory, especially for large d_0.

Figure 5 shows further comparisons with measurements, in this case on a perfectly smooth Dunlop SP3000 tyre with $d_0 = 60$ and 120 mm. There is no load on the tyre and d_0 is the measured distance from the microphone to the tyre/road contact point. The ability of the theory to describe variations in the listener's position is also tested in these plots. The listener is at (2·67 m, 15°) and (1·92, 2·4°) respectively.

The measured transfer functions share many similarities between the simplified cylindrical drum and the smooth tyre cases, confirming the initial geometrical modelling assumptions. The only minor difference is that the frequency dips of the interference patterns for the former are more clearly defined. The agreement between theory and experiment is excellent for frequencies higher than about 3 kHz, and the dependence on the listener's position is also correctly predicted.

The comparison with the predictions of the wedge theory shows that the tyre surface curvature significantly modifies the structure of the transfer functions and their magnitude. Generally speaking, the bandwidths of the spectral lobes are broadened and their magnitudes are reduced by the introduction of curvature. From the viewpoint of the ray theory, the change in lobe structure results from altered ray path lengths, and hence altered interference effects. The magnitude reduction arises because the curvature around the reflection point on the tyre increases the rate of area increase along the ray tube, and therefore the subsequent decay rate of the acoustic amplitude.

3. COMPACT TYRE MODEL

When the frequency is below about 100 Hz, the acoustic wavelength is much greater than the tyre diameter. The tyre can thus be modelled as a compact scatterer. The geometry of Figure 1 again applies, and the origin of co-ordinates is placed at the centre of the tyre/road contact line. The source then lies at $\mathbf{x}_s = (d_0, 0, 0)$, and the pressure field at a radian frequency Ω obeys the inhomogeneous Helmholtz equation

$$\left(\nabla^2 + \frac{\Omega^2}{c^2}\right) p = A\delta(\mathbf{x} - \mathbf{x}_s), \tag{10}$$

where $\mathbf{x} = (x, y, z)$, ∇^2 is the Laplace operator and A is the strength of the source. (Note that the harmonic variation $e^{-i\Omega t}$ has been suppressed.) The equation is to be solved subject to the boundary condition of zero normal velocity on the road and tyre surfaces, i.e.,

$$\frac{\partial p}{\partial n} = 0, \tag{11}$$

where n is the normal co-ordinate in the direction outward from the solution domain. The scattered acoustic waves must also be outgoing in the far-field, to satisfy causality.

The scattered waves can be found by expressing the far field pressure in the form of an integral equation involving a Green function. The Green function chosen is the wave field at $\mathbf{x}$ due to a point monopole source of unit strength at $\mathbf{x}' = (x', y', z')$, with an infinite rigid flat surface on $z = 0$. This function is the solution of

$$\left(\nabla^2 + \frac{\Omega^2}{c^2}\right) G(\mathbf{x}; \mathbf{x}') = \delta(\mathbf{x} - \mathbf{x}'), \tag{12}$$

subject to the boundary condition

$$\frac{\partial G}{\partial z} = 0 \tag{13}$$

on $z = 0$. It corresponds to the field of the source in free space, modified by that of an image source at $\mathbf{x}'_I = (x', y', -z')$, i.e.,

$$G(\mathbf{x}; \mathbf{x}') = -\frac{1}{4\pi}\left(\frac{e^{i\Omega|\mathbf{x}-\mathbf{x}'|/c}}{|\mathbf{x} - \mathbf{x}'|} + \frac{e^{i\Omega|\mathbf{x}-\mathbf{x}'_I|/c}}{|\mathbf{x} - \mathbf{x}'_I|}\right). \tag{14}$$

On multiplying equation (10) by G and performing a volume integral over $\mathbf{x}$, it becomes

$$\int_{z>0} GV^2 p \, \mathrm{d}^3\mathbf{x} + \frac{\Omega^2}{c^2} \int_{z>0} Gp \, \mathrm{d}^3\mathbf{x} = p_{free}, \tag{15}$$

where

$$p_{free} = -\frac{A}{4\pi}\left(\frac{\mathrm{e}^{\mathrm{i}\Omega|\mathbf{x}'-\mathbf{x}_s|/c}}{|\mathbf{x}'-\mathbf{x}_s|} + \frac{\mathrm{e}^{\mathrm{i}\Omega|\mathbf{x}'-\mathbf{x}_{sI}|/c}}{|\mathbf{x}'-\mathbf{x}_{sI}|}\right) \tag{16}$$

is the pressure field which the source of equation (10) would generate in the absence of the tyre. (Note that the relation $|\mathbf{x}'_I - \mathbf{x}_s| = |\mathbf{x}' - \mathbf{x}_{sI}|$ has been used to write it in this recognizable form.) The final equation for the pressure field then follows from applying the Green theorem [7] to the first term in equation (15) and invoking equations (11), (12) and (13). The result is

$$p(\mathbf{x}') = p_{free} + \int_S p(\mathbf{x}) \frac{\partial G}{\partial n} \, \mathrm{d}^2\mathbf{x}. \tag{17}$$

The modification of the acoustic field due to the existence of the tyre is thus represented by an integral incorporating the, as yet unknown, pressure on the tyre surface, S. A solution to equation (17), subject to the low–frequency condition $\Omega R/c \ll 1$, is now sought.

The derivative $\partial G/\partial n$ in equation (17) is equal to $\nabla G \cdot \mathbf{n}$, where $\mathbf{n}$ is the unit vector in the n-direction, and

$$\nabla G = -\frac{1}{4\pi}\left[\frac{\mathbf{x}-\mathbf{x}'}{|\mathbf{x}-\mathbf{x}'|^3}\left(\frac{\mathrm{i}\Omega}{c}|\mathbf{x}-\mathbf{x}'| - 1\right)\mathrm{e}^{\mathrm{i}\Omega|\mathbf{x}-\mathbf{x}'|/c}\right.$$

$$\left. + \frac{\mathbf{x}-\mathbf{x}'_I}{|\mathbf{x}-\mathbf{x}'_I|^3}\left(\frac{\mathrm{i}\Omega}{c}|\mathbf{x}-\mathbf{x}'_I| - 1\right)\mathrm{e}^{\mathrm{i}\Omega|\mathbf{x}-\mathbf{x}'_I|/c}\right]. \tag{18}$$

In the cases of practical interest, the observer is in the far field ($\Omega|\mathbf{x}'|/c \gg 1$), and this condition can be combined with the low–frequency requirement (which implies $\Omega|\mathbf{x}|/c \ll 1$ and hence also $|\mathbf{x}| \ll |\mathbf{x}'|$, for $|\mathbf{x}|$ on the tyre surface) to obtain

$$\nabla G \simeq \frac{1}{4\pi}\frac{\mathrm{i}\Omega}{c}\frac{(\mathbf{x}'+\mathbf{x}'_I)}{|\mathbf{x}'|^2}\mathrm{e}^{\mathrm{i}\Omega|\mathbf{x}'|/c}. \tag{19}$$

Under this approximation, equation (17) becomes

$$p(\mathbf{x}') = p_{free} + \frac{1}{4\pi}\frac{\mathrm{i}\Omega}{c}\mathrm{e}^{\mathrm{i}\Omega|\mathbf{x}'|/c}\frac{\mathbf{x}'+\mathbf{x}'_I}{|\mathbf{x}'|^2}\cdot\int_S p(\mathbf{x})\mathbf{n}(\mathbf{x}) \, \mathrm{d}^2\mathbf{x}. \tag{20}$$

This equation shows that the scattered field is due to the net force exerted on the tyre by the acoustic pressures. It thus exhibits the characteristic directivity pattern of a dipole, with two maxima and two minima. The directivity arises from the dot product of the force vector with the horizontal observer direction, $\mathbf{x}' + \mathbf{x}'_I$. For the source location chosen, symmetry

dictates that the force has no component in the y direction, and the maxima thus lie directly fore and aft of the tyre, with the minima at the sides.

The problem has now been reduced to finding the force on the tyre. Since it is compact, the local velocity field is effectively incompressible, and hence the pressure satisfies

$$\nabla^2 p = A\delta(\mathbf{x} - \mathbf{x}_s), \tag{21}$$

subject to the same boundary condition (equation (11)) as previously.

One could apply the standard incompressible boundary element method to solve this equation numerically and hence obtain the surface pressure on the tyre. However, a more convenient way to calculate the tyre force is by the use of a geometric potential. The potential $\Psi_x(\mathbf{x})$ is defined so that it satisfies the homogeneous Laplace equation

$$\nabla^2 \Psi_x = 0 \tag{22}$$

and the boundary condition

$$\frac{\partial \Psi_x}{\partial n} = \mathbf{n} \cdot \mathbf{e}_x \tag{23}$$

on the tyre and road surfaces. (Here $\mathbf{e}_x$ is the unit vector in the x direction.) The benefit of introducing Ψ_x can be seen by multiplying it with equation (21) and integrating over the volume $z > 0$. After the application of the Green theorem, one obtains

$$\mathbf{e}_x \cdot \int_S p(\mathbf{x})\mathbf{n}(\mathbf{x})\, \mathrm{d}^2\mathbf{x} = -A\Psi_x(\mathbf{x}_s). \tag{24}$$

In other words, the force in the x direction induced on the tyre by a point source at $|\mathbf{x}_s|$ is simply the value of the geometric potential at $\mathbf{x}_s$, multiplied by the source strength.

An integral equation for the geometric potential can be derived by using the same, Green function, approach that led to equation (17) for the acoustic pressure. The corresponding (incompressible) Green function satisfies equations (12) and (13) with $\Omega/c = 0$, and is given by

$$G_i(\mathbf{x}, \mathbf{x}') = -\frac{1}{4\pi}\left(\frac{1}{|\mathbf{x} - \mathbf{x}'|} + \frac{1}{|\mathbf{x} - \mathbf{x}'_I|}\right). \tag{25}$$

Combining this solution with (22) in the same way as previously then gives

$$\Psi_x(\mathbf{x}') = \int_S \Psi_x(\mathbf{x}) \frac{\partial G_i}{\partial n}\, \mathrm{d}^2\mathbf{x} - \int_S G_i \mathbf{n} \cdot \mathbf{e}_x\, \mathrm{d}^2\mathbf{x} \tag{26}$$

(cf., equation (17)). The unknown values of Ψ_x on the tyre surface are found by letting $\mathbf{x}'$ approach the tyre surface. This process is complicated by the singularity in G_i at $\mathbf{x}' = \mathbf{x}$, but can be shown to yield a finite result (see, for example, reference [6]). Hence one obtains an integral equation for the potential Ψ_x on the tyre surface:

$$\frac{\Psi_x(\mathbf{x}')}{2} = \text{p.v.} \int_S \Psi_x(\mathbf{x}) \frac{\partial G_i}{\partial n}\, \mathrm{d}^2\mathbf{x} - \int_S G_i \mathbf{n} \cdot \mathbf{e}_x\, \mathrm{d}^2\mathbf{x}, \tag{27}$$

where p.v. denotes the Gaussian principal value of the integral.

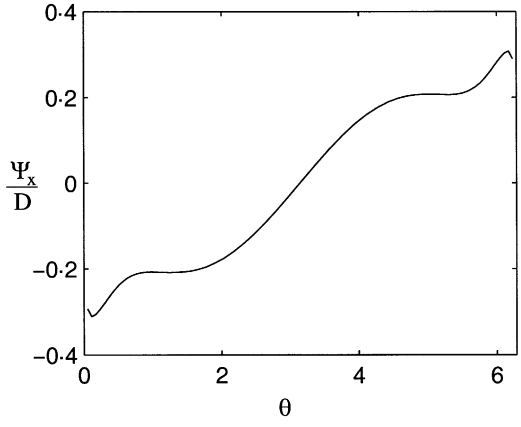

Figure 6. Geometric potential on the tyre belt. $w/D = 0{\cdot}333$.

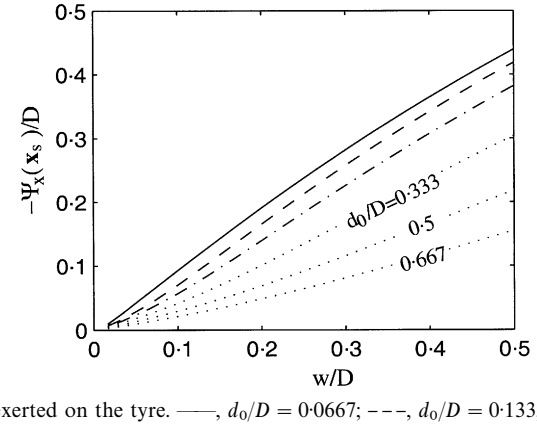

Figure 7. Force exerted on the tyre. ——, $d_0/D = 0{\cdot}0667$; – – –, $d_0/D = 0{\cdot}133$; – · –, $d_0/D = 0{\cdot}20$.

This equation has been solved numerically, on the mesh sketched in Figure 1. A typical solution for $\Psi_x(\mathbf{x}')$ on the tyre belt surface is shown in Figure 6. It is non-dimensionalized on the tyre diameter, D $(= 2R)$, which is about 0·6 m for common passenger car tyres.

The force exerted on the tyre can now be calculated by substituting the known boundary values of Ψ_x into equations (26) and (24). Figure 7 shows the force due to a source of unit strength as a function of the tyre aspect ratio, w/D, and source location. Over the range of aspect ratios plotted, the force on the tyre increases almost linearly with belt width, due to the stronger reaction force associated with the wider tyre belt. In contrast, the force decreases as the source moves away from the contact because the interaction between the source and the tyre weakens. Remarkably, there is effectively no dependence on the diameter, D.

The amplification due to the tyre can now be found by dividing equation (20) by p_{free}, and noting that $p_{free} \simeq -(A/2\pi|\mathbf{x}'|)e^{i\Omega|\mathbf{x}'|/c}$ in the far field. The result is

$$\frac{p(\mathbf{x}')}{p_{free}} = 1 + \frac{i\Omega D}{c}\frac{x'}{|\mathbf{x}'|}\frac{\Psi_x(\mathbf{x}_s)}{D}. \tag{28}$$

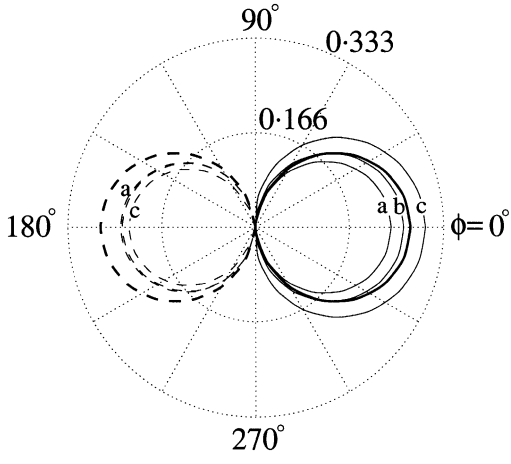

Figure 8. The dipole pattern on a linear scale. $w/D = 1/3$, $d_0/D = 0{\cdot}083$ and $\theta = 89{\cdot}4°$. ——, positive values of B; – – –, negative values of B. Simulation curves: (a) 20 Hz; (b) 50 Hz; (c) 100 Hz.

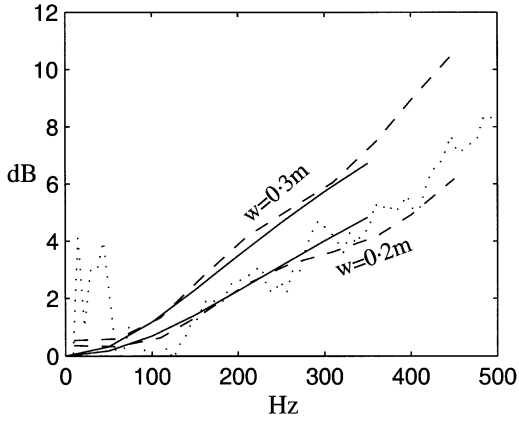

Figure 9. Transfer functions at low frequencies. ——, compact multipole expansion; – – – boundary element method; ···· experimental measurement.

The dipolar dependence of the scattering term can be made explicit by defining

$$B(\theta, \phi) = -\frac{x'}{|\mathbf{x}'|}\frac{\Psi_x(\mathbf{x}_s)}{D} = -\frac{\Psi_x(\mathbf{x}_s)}{D}\sin\theta\cos\phi, \tag{29}$$

where θ is the angle from $\mathbf{x}'$ to the z-axis and ϕ is the horizontal projection angle of $\mathbf{x}'$ to the x-axis. The low frequency prediction for B is compared with the BEM simulation in Figure 8. The theoretical results are shown by the thick lines, and are symmetrical fore and aft. Among the calculation results, a symmetric dipole is evident for the lowest frequency shown, 20 Hz, with amplitude about 16% smaller than the theoretical prediction. As the sound frequency increases, the dipole lobe structure becomes biased towards the front of the tyre. This is due to contributions from higher order multipole sources.

The ability of the theory to predict low frequency horn amplification is demonstrated in Figure 9. Here transfer functions at an observer location $(L, \phi) = (3{\cdot}16\text{ m}, 30°)$ are plotted

for a source 100 mm from a 0·6 m diameter tyre. Two widths are tested, 0·2 m, for which theoretical, experimental and BEM results are shown, and 0·3 m, where only theoretical and BEM results are available. The agreement is excellent up to about 300 Hz ($\Omega D/c \simeq 3{\cdot}3$).

4. CONCLUSIONS

In this paper, two asymptotic theories for sound amplification by a tyre/road geometry have been presented. The first (section 2) is based on the Keller ray theory [4], and shows good agreement with experiment at high frequencies (above 3 kHz for a representative geometry). The second (section 3) is a low frequency analysis, and compares well with experiment and BEM computations up to 300 Hz (for the representative geometry).

The ray theory has two attractive features. Firstly, it gives predictions of the amplification at frequencies beyond the practical reach of BEM calculations (see Figures 4 and 5). Secondly, it provides a useful physical basis for the interpretation of the lobed interference patterns seen at these frequencies. When compared with an earlier model, Ronneberger's [1] wedge representation (which leads to an image source formulation), the ray theory locates the frequency minima more accurately, and shows that Ronneberger's amplitude predictions are much too high (because they neglect additional ray spreading due to reflection by the curved tyre surface).

The low frequency theory also provides useful quantitative information, in a range where accurate experimental results are hard to obtain. However, as BEM calculations are inexpensive at these frequencies, its main strength is the insight it yields into the parametric dependence of the amplification. Specifically, equation (28) and Figure 7 show that it is effectively independent of tyre diameter, and is approximately given by

$$1 + \left(\frac{\Omega w}{c} \sin\theta \cos\phi \right)^2$$

for a source close to the tyre. (Here w is the tyre width, and the angles θ, ϕ specify the observer location via equation (29).) This expression appears to be valid up to $\Omega w/c \simeq 1{\cdot}5$.

In summary, at low and high frequencies it is possible to describe the horn effect with asymptotic theories which not only give good quantitative predictions, but also illuminate the physical aspects of the phenomenon. Equally, this work also shows that, at the frequencies of practical interest for tyre noise (approximately 500–2500 Hz), a numerical approach is required to predict the amplification accurately.

ACKNOWLEDGMENTS

This research was undertaken with support from EPSRC under the Inland Surface Transport Link Programme. It has been carried out in collaboration with Dunlop Tyres Ltd., TRL and the Landrover Group, UK, whose contributions and interest are gratefully acknowledged.

REFERENCES

1. D. RONNEBERGER 1989 *Workshop on rolling noise generation, Institut fur Technische Akustik, Technische Universitat Berlin.* Towards quantitative prediction of tyre/road noise.

2. R. A. G. GRAF, C.-Y. KUO, A. P. DOWLING and W. R. GRAHAM 1999 *Proceedings INTERNOISE Conference* 1999, *Ft. Lauderdale*. Horn amplification at a tyre/road interface—Part I: experiment and computation.
3. R. A. G. GRAF, C.-Y. KUO, A. P. DOWLING and W. R. GRAHAM 2002 *Journal of Sound and Vibration* On the horn effect of a tyre/road interface, Part I: experiment and computation.
4. J. B. KELLER 1957 *Journal of Applied Physics* **28**, 426–444. Diffraction by an aperture.
5. C.-Y. KUO, R. A. G. GRAF, A. P. DOWLING and W. R. GRAHAM 1999 *Proceedings INTERNOISE Conference* 1999, *Ft. Lauderdale*. Horn amplification at a tyre/road interface—Part II: ray theory and experiment.
6. R. D. CISKOWSKI and C. A. BREBBIA, editors 1991 *Boundary Element Methods in Acoustics*. London: Elsevier Applied Science.
7. G. ARFKEN 1985 *Mathematical Methods for Physicists*. London: Academic Press.

APPENDIX A: RAY THEORY

Ray theory [4] is a representation of the wave equation that is valid at high frequencies. According to this theory, sound travels along line paths, or 'rays', whose geometry is independent of frequency. When the ambient fluid has uniform sound speed and mean density, the rays are straight lines unless they are reflected by boundaries, such as the tyre and road surfaces. Edge scattered waves represent a higher order correction [4], and hence are neglected.

Assume a straight ray with time dependence $e^{-i\Omega t}$ and wavenumber k ($= \Omega/c$). The corresponding pressure can be expressed as $p(s) = A(s)e^{iks}$, where s is the distance measured along the ray, with associated amplitude $A(s)$ and phase ks. Neighbouring rays form a 'ray tube', as shown in Figure A1. It can be shown that acoustic energy flux is conserved along this tube [4]. Therefore, $A^2(s)\,d\Sigma(s)/\rho c$ is a constant, where $d\Sigma(s)$ is the cross–sectional area of the ray tube. The elemental area $d\Sigma(s)$ has two Gaussian principal directions, say 1 and 2, and principal radii of curvature $\sigma_1 + s$ and $\sigma_2 + s$ respectively. Physically, σ_1 and σ_2 are the distances from $s = 0$ to the 'caustics' (centres of curvature) of the two principal directions. Therefore, the ratio of the area change, $d\Sigma(s)/d\Sigma(0)$, is $(\sigma_1 + s)(\sigma_2 + s)/(\sigma_1\sigma_2)$, which implies that the ray amplitude at s is given by

$$A(s) = A(0)\left(\frac{\sigma_1\sigma_2}{(\sigma_1 + s)(\sigma_2 + s)}\right)^{1/2}. \tag{A1}$$

Ray reflection (Figure A2) is specular and, for rigid a surface, conserves acoustic energy while leaving the phase of the ray unaltered. Thus, when the incident ray from the caustic S is reflected, one can imagine that the subsequent ray is emitted from the image caustic S' with an amplitude which corresponds to $p(0)$ at point O. Therefore, incorporating (A1), the ray at s is described by

$$p(s) = p(0)\left(\frac{\sigma_1\sigma_2}{(\sigma_1 + s)(\sigma_2 + s)}\right)^{1/2}\exp(iks), \tag{A2}$$

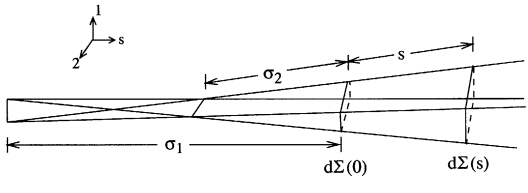

Figure A1. A ray tube. s is the distance along the ray measured from the element area $d\Sigma(0)$. σ_1 and σ_2 are the distances from $s = 0$ to the caustics in the Gaussian principal directions 1 and 2.

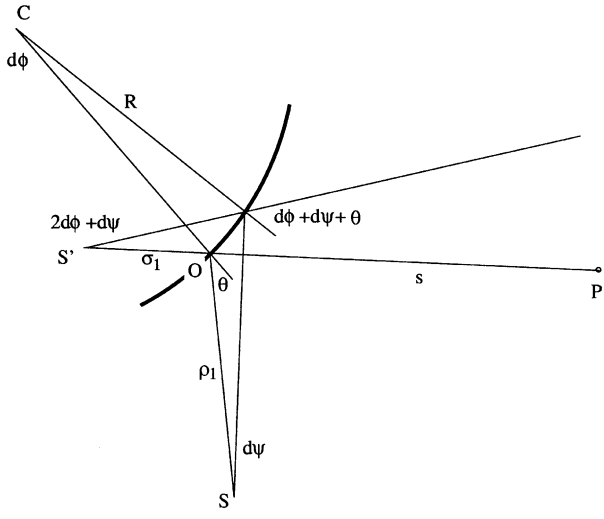

Figure A2. Ray reflection by a smoothly curved surface with radius of curvature R.

where σ_2 is the distance from O to the caustic of the ray in the second principal direction (perpendicular to the plane of Figure A2). From elementary geometrical considerations, one has $R\,\mathrm{d}\phi\cos\theta = \sigma_1(2\mathrm{d}\phi + \mathrm{d}\psi) = \rho_1\mathrm{d}\psi$, and hence $\sigma_1 = \rho_1 R\cos\theta/(2\rho_1 + R\cos\theta)$. In the out-of-plane direction, $\sigma_2 = \rho_2$ (because the radius of curvature is infinitely large across the belt for this cylindrical tyre). Equation (A2) can thus be applied successively to calculate the ray amplitude after each reflection on the tyre belt and road.